Engineering Geology 123 (2011) 91–99

Contents lists available at ScienceDirect

Engineering Geology

journal homepage: www.elsevier.com/locate/enggeo

Landslide-induced levee failure by high concentrated sediment flow — A case of Shan-An levee at Chenyulan River, Taiwan

Ming-Der Yang [a], Ji-Yuan Lin [b,*], Chia-Yao Yao [c], Jen-Yan Chen [a], Tung-Ching Su [d], Chyan-Deng Jan [e]

[a] Department of Civil Engineering, National Chung Hsing University, Taichung, Taiwan 402, R.O.C.
[b] Department of Construction Engineering, Chaoyang University of Technology, Taichung, Taiwan 413, R.O.C.
[c] The 4th River Basin Management Bureau, Water Resources Agency, Ministry of Economic Affair, Changhua, Taiwan 524, R.O.C.
[d] Department of Civil Engineering and Engineering Management, National Quemoy University, Kinmen, Taiwan 892, R.O.C.
[e] Department of Hydraulic and Ocean Engineering, National Cheng Kung University, Tainan, Taiwan 701, R.O.C.

ARTICLE INFO

Article history:
Accepted 27 July 2011
Available online 4 August 2011

Keywords:
Outcrop investigation
Remote sensing
Scenario simulation
Flooding
Levee failure

ABSTRACT

Typhoon Mindulle struck northeast Taiwan on July 2, 2004, and brought an abundant air current in the following days that caused serious flood disasters to the mountainous areas in central Taiwan. One of sever flood events during Typhoon Mindulle was about hundreds of hectares of farmland loss induced by an 1620 m break of Shan-An levee at the Chenyulan River. This paper examines the nature and causes of Shan-An flood by integrating catastrophic investigation and scenario simulation. The catastrophic investigation of the disaster scene, including field survey, outcrop investigation, and remote sensing image interpretation, was executed to reveal the inundation for disaster response and recovery. SPOT-IV and FORSAT-II satellite images and airborne images provided temporal and spatial information for inundation investigation. The HEC-RAS hydraulic model was applied to estimate the water surface profiles of Shan-An levee around the lower reach of Chenyulan River. Also, the impacts of debris and water in the hyper-concentrated sediment flow were estimated to illustrate the effects of sediment yield on Shan-An levee. The result shows that the levee was designed to sustain the heavy rainfall bought by Typhoon Mindulle but failed to the impact of high concentrated sediment flow induced by sediment yield from the landslide. The seismic-triggered landslide on the left riverside was reactivated by intensive rainfalls to deposit a great amount of sediments on the riverbed that narrowed down the river width, increased the impact force, and diverted water toward Shan-An levee. The levee failure should draw more attention from engineers while designing a new flood control structure in the waterway of Chenyulan River due to the occurrence of the hyper-concentrated sediment flow and landslide residuals after the Chi-Chi earthquake (M_L 7.3). In addition, the perceived investigation and analysis of an earthen levee failure provides essential information to setup a proper recovery plan of Shan-An levee and a basin management strategy of Chenyulan River in the future.

1. Introduction

Being located in a sub-tropic area, Taiwan faces serious attacks from several typhoons during a Summer–Autumn season, and has a mean precipitation of 2500 mm/year and even up to 3000 mm/year in the central mountainous area. Last decades, almost every year Taiwan experienced seasonal disasters induced by typhoons which caused a serious threat to human life and property. Periodic flooding becomes a critical natural hazard so that the authorities have been devoted to disaster prevention and mitigation. Most of the serious floods occurred in central Taiwan, especially within Jhuoshuei River basin which is the second largest watershed in Taiwan. In an effort to address the flooding problem, the authority The Fourth River Basin Management Bureau commissioned to study the situation to come up with effective and practicable strategies for future structural design and improvement of drains within this area to control periodic flooding.

However, the mechanism of flood becomes complex nowadays. Besides a great amount of rainfall, landslides, which could be caused by river scour or heavy rainfall, are considered as another major factor inducing or exaggerating flood events. For example, Forecasting of Landslides Induced by Rainfalls (FLaIR) hydrological model was applied to correlate the rainfall amount and landslide or mudflow movement occurrences in Sarno, Southern Italy (Sirangelo and Braca, 2004). The triggering mechanism of the reservoir-induced landslide in Maoping on the left bank of the Qingjiang River, China, which resulted in relocation of a village of 290 people, was examined based on field investigation of the constituent structure and geological formation (Qi et al., 2006). Landslides in Clyde Dam reservoir, New Zealand, which were observed by a combination of inclinometers, extensometers and survey and correlated with controlling events

* Corresponding author. Tel.: +886 4 23323000x4007; fax: +886 4 23742325.
E-mail address: jylin@mail.cyut.edu.tw (J.-Y. Lin).

0013-7952/$ – see front matter © 2011 Elsevier B.V. All rights reserved.
doi:10.1016/j.enggeo.2011.07.006

including lake filling, storms, floods, prolonged wet periods and earthquakes, were found to increase their movement rates following prolonged rainfall events (Macfarlane, 2009). In the above cases, both perceived and modeling approaches were employed for the cause identification of landslide-induced flood event. This paper also applies a hydraulic model, remote sensing data, and field investigation to reveal the cause of landslide-induced levee failure and inundation.

Remote sensing techniques coupled with simulation models have been confirmed in identification, prevention and monitoring, and assessment of individual natural disaster. Satellite and airborne images are important data sources for scenario simulations of natural disasters, which are valuable to damage prevention by avoiding human settlements in unsuitable area (García-Meléndez et al., 1998; van der Sande et al., 2003). Various studies have shown that remote sensing data are spatially and temporally efficient in inundation investigation (Knebl et al., 2005; Pappenberger et al., 2005; Yang et al., 2007). Integration of remote sensing and scenario simulation can be a low-cost and efficient method providing critical information for decision support of disaster prevention and reduction to emergency managers and the disaster response community for disaster management (Montoya, 2003; Bisson et al., 2005; Teng et al., 2005; Tralli et al., 2005). This paper employs remote sensing data acquired from SPOT-IV and FORMOSAT-II satellites and airborne to identify the terrain change caused by flooding and the inundation area.

To avoid the repetition of the disasters in the future, this research focuses on a flood investigation by integrating remote sensing for mapping flood zones and scenario simulation for resolving the major causes of the levee collapse in the Shan-An flood during the flood event of 2nd July, 2004. A thorough review of disaster area identification, disaster cause analysis, and a constructive suggestion for the future recovery projects were addressed in this paper.

2. Study site: Chenyulan River

Jhuoshuei (meaning turbid water in Chinese) River is the longest (186.6 km) river in Taiwan and has a drainage area of 3157 km^2. Chenyulan River is the major branch of Jhuoshuei River, originates from Yushan Mountain, which is Taiwan's highest mountain (3910 m above sea level), and has a main stream about 42.40 km, a drainage area of 450 km^2, and 6 main tributaries, including Jung-Kun River, Neimoupu River, Shihbachong River, Niouchou River, Heshe River, and Shalisian River (see Figure 1). With an average slope gradient of 1/20 throughout the whole drainage area, a supercritical flow often appears. In the supercritical state, waves are swept downstream and a small obstruction can create a wedge-shaped wave, and the flow has a high velocity and is usually described as rapid, shooting, and torrential (Chow, 1973).

Besides, the Chi-Chi earthquake (M_L 7.3) on 21 September 1999 was the largest natural disaster in Taiwan for last centenary and shook the formations of mountains and rivers in central Taiwan. Thousands of landslides were mapped through SPOT images in Jhuoshuei River basin draining much of the epicentral area (Dadson et al., 2004).

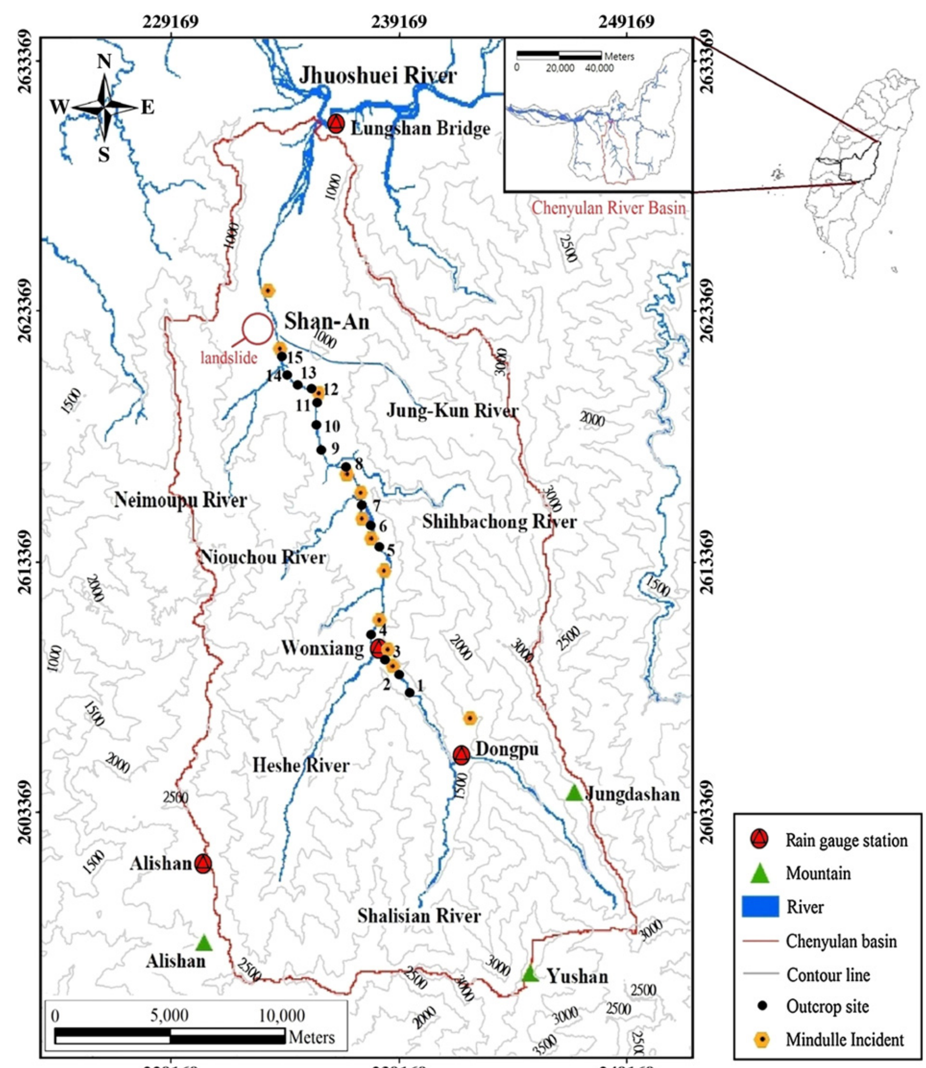

Fig. 1. The Chenyulan River basin. The elevation drops from >3000 m to <1000 m within 42.40 m of a river length.

Heavy rainfalls added new impetus to the situation so that an averaged erosion rate of 3–7 mm/year and mostly up to 60 mm/year was caused by the combination of tectonic and climatic effects (Dadson et al., 2003). Following the Chi-Chi earthquake, a 4.4-fold increase of sediment concentration in Chenyulan River was observed by calculating unit sediment concentration from a log-transformed least-squares regression function (Dadson et al., 2004). According to the pre- and post-seismic suspended-sediment rating curves combining suspended-sediment concentration and water discharge, the suspended-sediment discharge of Jhuoshuei River increased comparably by a factor of 2.65 to 143 Mt/year based on the averaging 54 Mt/year before earthquake (Dadson et al., 2004). Many coseismic landslides remained confined to hillslopes, and more silts are expected to be carried by surface water downstream from the erosion areas (Yu et al., 2006). Silting up of riverbed and banks has caused a remarkable rise in the flood level to decrease the flood discharge capacity of Chenyulan River.

Increasing population and agricultural activities along the river required more waterway constructions for flood protection. However, the man-made flood control structures, such as river embankments and retaining basins, affect flooding characteristics. Chenyulan River has been significantly leveed so that much more sediment was deposited onto the riverbed. The worsening flood risk in the Chenyulan basin is not only a natural process but also the result of inappropriate human intervention in its drainage basin. Vegetation destruction and soil erosion in the watershed, shrinking water retaining areas, restriction of channel capacity could be reasons of levee destruction. The high frequency and long duration of flooding are accentuated by the deteriorating topography and human intervention. In consequence, flood disasters have brought untold hardships to residents, industrial developers, tourists and owners of tourism businesses in this area.

3. Field and outcrop investigations of Mindulle flood

A major rainy season extends from May to September with 91% of a mean annual rainfall (2182 mm/2400 mm) based on the record of Wonxiang rain gauge station. Chenyulan River was battered by typhoons and tropical storms last decay as shown in Fig. 2. Of those events, Typhoon Mindulle induced the most serious catastrophe by unexpectedly huge amounts of rainfall to central Taiwan. The rescuers battled mudslides and muddy flood waters to successfully evacuate 295 trapped villagers in 51 mountainous regions in central Taiwan. More than 10,000 people were evacuated from susceptible districts to the shelters nearby. Many residents in the mountainous regions stayed at concentrated shelters for several weeks. Typhoon Mindulle stalled for only 8 h on the island, but the following rainfall incurred over 0.3 billion US dollars in property damages and 33 deaths. Following Typhoon Mindulle hitting Taiwan on 2nd July 2004, Taiwan Central Weather Bureau continually issued heavy rainfall warning due to outer circulation of tropical depression that caused a severe catastrophe in Chenyulan River. The temporal extent of the study was selected as July 2–5 2004 as the duration of storm brought by Mindulle.

During July 2–5, the Chenyulan River received an intensive rainfall at about 1715 mm in one single event as shown in Fig. 2, which was approaching one half of yearly rainfall (3300 mm) at Alishan rain gauge station. Several comparable flood extents occurred at the right lateral riverbank of Chenyulan River where there are many villages beside, such as Shan-An village. The Shan-An levee had been affected by a series of damaging events and had been rebuilt (Chen et al., 2006). The failure chronology of Shan-An levee (officially including both Shan-An levee and Jung-Kun levee) is listed in Table 1.

A comprehensive disaster investigation is an essential reference for disaster recovery planning, which includes rebuilding disaster areas, reconstituting government operations, and helping individuals and communities to return to normal (FEMA, 2006). Within the days following Typhoon Mindulle, several groups of field observers and

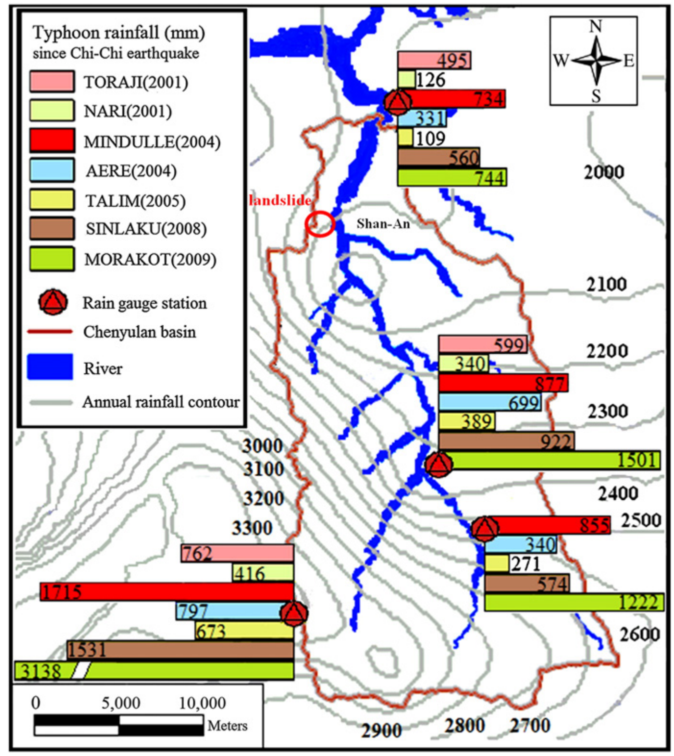

Fig. 2. Precipitation of Chenyulan River basin during the historical events after Chi-Chi earthquake.

investigation crews were deployed to interview residents. The survey crews equipped with kinematic GPS with digital maps to accurately locate the incidents were assembled to survey the disaster extent. Moreover, interviewing residents, finding on-site evidence of incidents, taking digital photographs and video tapes, roughly verifying the type of destruction, and determining the instant need at the incident sites were required. Several destructive incidents occurred along the Chenyulan River in the Mindulle event whose locations are shown in Fig. 1. Several levees protecting farming and living areas on the sides of Chenyulan River failed, in which the failure of Shan-An levee caused the most serious catastrophe. The interview with local residents revealed that the failure of earthen levees occurred at about 10 AM on the 3rd of July and started between Sections 17.1 and 18, and consequently floodwalls passed the Shan-An terrace on the east side of Chenyulan River with about 2 m of standing water and more than 100 ha of inundated area.

The valley along Chenyulan River is a typical fault-line valley. Chenyulan Fault, closely along Chenyulan River (see Figure 3), is a boundary fault separating the Neogene sedimentary rocks of the Western Foothills on the western side from the Paleogene metamorphic rocks of the Hsuehshan Range on the eastern side. Rock masses of the Chenyulan watershed are highly fractured due to faulting and folding. The soil of landslide area is unconsolidated and in modern alluvial deposition, containing large boulders, cobbles, gravels, sand, silt and clay.

Table 1
Historical failure of Shan-An levee.

Event	Date	Rainfall (mm)/M_L[a]	Failure length (m)
Typhoon Ofelia	June 21–24, 1990	131	75
Typhoon Yancy	August 17–20, 1990	425	264
Typhoon Doug	August 6–9, 1994	492	100
Typhoon Herb	July 29–August 1, 1996	808	480
Typhoon Zeb	October 13–17, 1998	297	120
Chi-Chi earthquake	September 21, 1999	7.3	802
Typhoon Mindulle	June 28–July 3, 2004	781	1620

[a] M_L: Richter magnitude.

Outcrop investigation was implemented by sampling the sediment of one cubic meter (1 m × 1 m × 1 m) on the surface of the riverbed at 15 ordinary sampling sites along Chenyulan River as shown in Fig. 1. Sieve analysis was processed *in situ* and in laboratory for the particle size larger and less than 3/8 inch (9.5 mm), respectively. Table 2 shows the characteristics of the riverbed material samples that most of the sediments are gravels (34.1% to 74.2% by weight), and followed by cobbles (8.9% to 34.8%), boulders (0.8% to 23.0%), and sand (9.3% to 25.6%). All 15 sampling sites contain little silt and clay (particle < 0.06 mm) under 3.1%. In Table 2, the sorting coefficient S_o is a sorting index of describing the distribution of grain sizes in a sample of unconsolidated material and is defined as $\sqrt{D_{75}}/\sqrt{D_{25}}$, in which D_{75} and D_{25} are the diameters such that 75% and 25% material by weight is finer than these sizes respectively. For a river section with a steady flow, S_o is small and classified as well-sorted to represent uniform particle of the riverbed in size. Among the 15 samples, 9 sites (60%) were classified into poor-sorted (S_o larger than 4.0), 6 sites (40%) were classified into fair-sorted (S_o between 2.5 and 4.0), and none was well-sorted (S_o less than 2.5). The velocity of a high concentrated flow suddenly decreases at the abrupt widening sections, such as outcrop site Nos. 8, 9, 10, and 14, so that a great amount of debris sink and settle inferred by comparatively large S_o or poor-sorted. The particle size distribution of Chenyulan River shown in Fig. 4 reveals the sorting coefficient decreasing with the upper (the steepest curve), middle, and lower reaches. The upper and lower boundaries represent the maximum and minimum of grain size distribution. Significantly unsteady flow of Chenyulan River results in a poor-sorted riverbed that becomes the sources of high concentrated sediment flow during a flood event.

4. Image process of remote sensing data

To make a correct strategy of disaster response and recovery, acquisition of precise updated information is essential. Satellite images and aerial photographs were acquired to identify the flooding zone and damage assessment. Low-altitude aerial photographs were taken right after Mindulle and show an overall view of flooding severity in Fig. 5. Through photogrammetric process, an orthophoto mosaic was generated for an efficient disaster monitoring information, such as landslide relief, over a temporal and spatial scale (Hamandawana et al., 2005; Dewitte et al., 2008). In Fig. 6A and B, high-altitude aerial mosaics of Chenyulan River taken before and after Typhoon Mindulle give a sense of terrain change caused by the flood. The pre- and post-aerial photographs were taken in July 2003 and 2004 with a nominal scale of 1/8000, an elevation above mean sea level of 3600 m, and endlap of 65% and sidelap of 30%. Planimetric surveys at scale of 1/1000 were performed in order to document the spatial extent of stratigraphic units shown in Fig. 6B. Section 18 has a width of ~300 m with a left bank of natural sharp hill and a right bank of concrete surfaced earthen levee.

To establish a DEM (Digital Elevation Model) with an accuracy of 0.5 m in elevation, the photogrammetric procedure was applied to the photograph negatives which were scanned through Vexcel Ultrascan 5000 scanner with a pixel resolution of 20 μm. For comparison, DEMs reveal the elevation variation around Shan-An region for the pre- and post-flood Chenyulan River by using ArcView's Spatial Analyst extension. Based on the DEMs of the waterway, Fig. 7A shows the elevation change of riverbed. About 138,500 m^3 sediments were washed out and ~13 m sediments deposited to riverbank from the landslide situated on the slope hill of the opposite side of Shan-An levee. In addition, satellite image also assisted in mapping of the hazard areas and estimating the damages of the Shan-An residential suburb, including agricultural damages, broken traffic, and building or infrastructure destructions. The interpretation of the satellite images pre- and post-flood in Fig. 6C and D, respectively, were employed to identify the hazard areas and damages by image processing on ERDAS IMAGINE, including geometric and radiometric correction, NDVI (Normalized Difference Vegetation Index) analysis, and change detection. Due to the daily imaging, FORMOSAT-II imagery, which was launched in May 2004 by National Space Organization (NSPO) of Taiwan and provides timely and low-cost image data with a panchromatic image with the resolution of 2 m-resolution and multi-spectral images of 8 m-resolution, is the most valuable remote sensing data source for disaster monitoring because of its high temporal resolution (NSPO, 2005). A repeated observation through satellite imagery is suitable for the long-term follow-up program. For multi-temporal image analysis, three requirements include univariate at each temporal image, precise co-registration, and radiometric consistency (Piwowar et al., 1998), which were completed prior to analysis in this research. Near infrared (NIR) reflectance intensity is related most to vegetation biomass, which absorbs red light, and inversely to water content. Destroyed vegetation and water content caused by the flood reduced NIR reflectance intensity in the inundated terrains. NDVI in terms of the difference between NIR and red reflectance intensity ranges 1 and −1 to represent vegetation condition. Change detection was processed on NDVI maps derived from a SPOT-IV satellite image before the flood and FORMOSAT-II after the flood for inundation identification. The inundation map derived from satellite images and overlaid onto an aerial photograph represents an estimate of the topped farm of the inundated area of 157 ha and the sediment deposit area of ~40 ha shown in red in Fig. 7B. Most inundation area was vineyard that caused about a loss of 7.6 million US dollars based on the unit grape yield of 31 ton/ha.

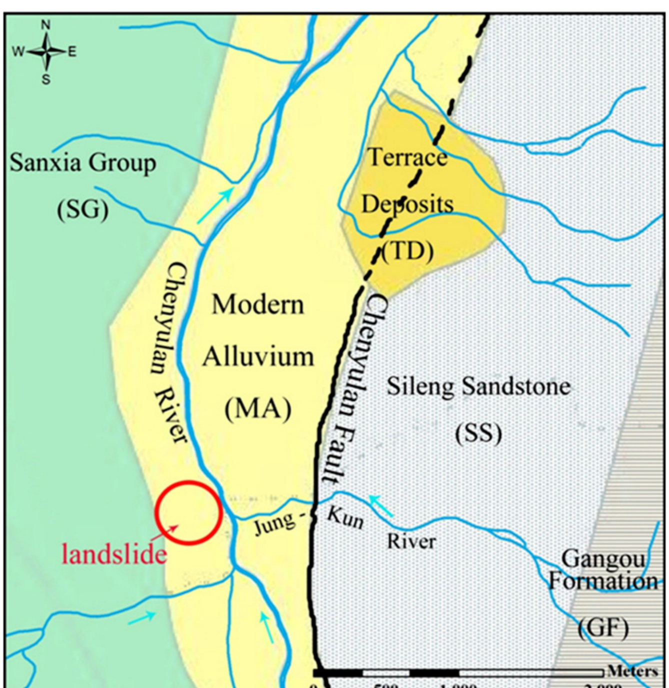

(MA): Alluvium, Modern.
(TD): Terrace deposits, Gravel, Soil and Sand, Pleistocene.
(SG): Sanhxia Group, Sandstone, and Shale, Late Miocene.
(GF): Gangou Formation, Argillite, Slate, and Phyllite, Oligocene to Miocene.
(SS): Sileng Sandstone, Alternation, Slate, and Coal Shale, Eocene to Oilgocene.

Fig. 3. Geological formation of Shan-An region in Chenyulan River.

5. Hydraulic simulation using HEC-RAS

It was under argument whether Shan-An levee was designed to resist the heavy rainfall brought by Typhoon. A hydraulic model HEC-RAS (Hydrologic Engineering Center's River Analysis System) version 3.1.2 developed by U.S. Army Corps of Engineers includes water surface profile

Table 2
Characteristics of the outcrop samplings in Chenyulan River.

Sampling no.	Mean particle size, D_m (mm)	Particle size (mm)					Maximum particle size, D_{max} (mm)	Boulder (%) particle size >256 mm	Cobble (%) particle size 256–64 mm	Gravel (%) particle size 64–2 mm	Sand (%) Particle size 2–0.06 mm	S_0 ($\sqrt{D_{75}}/\sqrt{D_{25}}$)
		D_{10}	D_{25}	D_{50}	D_{75}	D_{90}						
1	62.0	0.8	2.0	10.0	47.6	255.2	430.0	9.9	12.0	52.9	25.0	4.9
2	40.7	1.4	3.5	15.9	39.8	110.2	400.0	2.8	13.0	67.3	16.7	3.4
3	36.3	0.9	2.3	6.8	23.6	94.0	390.0	3.6	8.9	64.0	23.4	3.2
4	41.7	2.4	6.5	18.4	43.0	97.5	360.0	3.1	13.0	74.2	9.3	2.6
5	44.3	1.2	4.0	17.7	54.3	140.8	330.0	2.0	19.0	61.5	17.4	3.7
6	52.4	0.6	2.4	17.7	55.7	173.5	380.0	4.8	17.1	54.9	23.0	4.8
7	56.9	0.2	2.4	20.0	53.7	167.6	420.0	6.6	14.4	60.0	15.9	4.7
8	54.0	0.5	1.9	9.8	65.0	193.9	330.0	4.9	20.3	47.1	25.6	5.9
9	55.2	0.6	2.0	11.4	72.1	182.4	290.0	4.2	22.9	48.3	23.1	6.0
10	49.4	0.7	2.0	14.7	63.1	174.3	300.0	2.3	22.7	49.2	25.0	5.6
11	99.4	0.6	9.5	45.2	171.0	281.4	430.0	11.9	24.2	46.9	15.9	4.2
12	148.9	0.8	9.4	60.6	253.5	420.8	550.0	23.0	27.0	34.1	15.0	5.2
13	74.9	0.7	6.9	29.3	84.2	246.5	420.0	8.2	22.7	53.0	15.3	3.5
14	98.2	0.4	4.9	50.0	178.4	258.1	330.0	10.0	34.8	36.1	18.1	6.0
15	46.0	1.1	4.0	22.6	60.0	140.5	280.0	0.8	22.1	62.1	13.8	3.9

computations and bridge hydraulics was adopted to simulate one-dimensional unsteady flow for the Chenyulan River. HEC-RAS is able to simulate steady and unsteady flows, consider various hydraulic works, including bridges and storage areas, and facilitate hydraulic design (USACE, 2002). HEC-RAS river hydraulic model was proved to provide accurate and useful results in flooding related research by detecting the flooded areas for a discharge and flood hydrograph with a given return period (Pappenberger et al., 2005). The HEC-RAS simulation provides a water surface profile and cross-section mean velocity of the lower reach of Chenyulan River around Shan-An levee. The HEC-RAS input includes geometric data, such as river reach, junction, cross section, bridge, and inline weir, Manning's *n* value, flow data, and boundary conditions. The cross-section information was measured based on the planimetric shape derived from aerial photographs. According to the field investigation and the comparison between the riverbed situation (see Figure 5G) with the photographs of the typical channels in Chow's book (1973), Manning's *n* was estimated as 0.042 for the hydraulic simulation.

Within the Chenyulan watershed, there are four rain gauge stations, including Alishan, Donpu, Wonxiang, and Longshen Bridge (see Figure 1). According to the rainfall record and dimensionless unit hydrograph, the flow of Chenyulan River around Shan-An region was estimated during the flood event (July 2–5, 2004) as shown in Fig. 8. Two peak flows occurred at about 9 AM on the 3rd with 3200 cms and at 11 PM on the 4th with 4585 cms.

According to the witness interview, the failure of Shan-An levee started at about 10 PM on July 3 rd and between Section 17.1 and Section 18. At this time point, the estimated peak flow is about 3200 cms (about 10-year return period of 3130 cms) which is much less the design flow 5850 cms (100-year return period). The HEC-RAS result shows that the Shan-An levee should not be overtopped by a

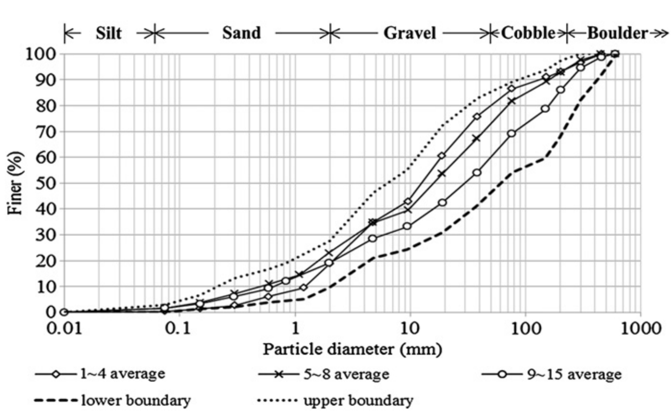

Fig. 4. Grain size distribution of Chenyulan riverbed.

flow of such magnitude as brought by Mindulle. It remains to be found other causes responsible for the failure of Shan-An levee.

Two observations were suspected of the levee destruction inducing the devastative flood. One is the elevated river bed due to the amount of sediment delivered from the watershed and deposited on the reach of Chenyulan River. More importantly, the diversion of river by the sediments from the landslide was caused by the slope base erosion and heavy infiltration. The following work emphasizes in analyzing the landslide failure and the flow impact force on Shan-An levee.

6. Landslide analysis and impact force estimation

6.1. Landslide analysis

The landslide at the left hillside opposite to Shan-An levee was suspected of the major cause inducing the levee failure during Typhoon Mindulle. The pre- and post-aerial photographs of the landslide in Fig. 9A and B were subset from Fig. 6A and B, respectively. A small landslide with a slope of 31° and oriented to the northeast in Fig. 9A was triggered first by Chi-Chi earthquake and identified by the comparison of satellite images taken before and after the earthquake. During the Mindulle event, the seismic-triggered landslide was reactivated by intensive rainfalls by means of two phenomena, such as (1) increasing infiltration resulted from surface runoff on the bare soil of the upper slope due to the seismic-induced landslide; and (2) the scoured toe of the slope by the storm flow as shown in Fig. 5E. Since the rock mass was very heavily broken, a circular rupture surface was formed. The drop in elevation depicts the break line of the landslide by comparing the pre- and post-DEMs in Fig. 9B. The volume change of the landslide can be estimated from the comparison of the DEMs. Based on the differential DEMs, a loss of volume of 138,500 m^3 and the maximum height of its rupture surface of 31 m were measured. Maps of ground displacements inferred form the comparison between the profiles of A–B cross-section extracted from the DEMs in Fig. 9C. Based on the equivalent mass of loss at the upper slope and deposit downslope, a run-out distance, which is defined as the horizontal distance from the toe of the sliding slope to the farthest deposit (Finley et al., 1999), of ~240 m blocking 80% river width at Section 18 was estimated during the Mindulle event, but only ~50 m deposit extent was left on the left riverbank after the flood. In result, the flow diverted toward the Shan-An levee at 20° was inferred to increase the impact force of the flow.

6.2. The impact force of water (F_w)

Several reports addressed that the inundation with much sediment yield resulted in severe flood disasters (Kawaike et al.,

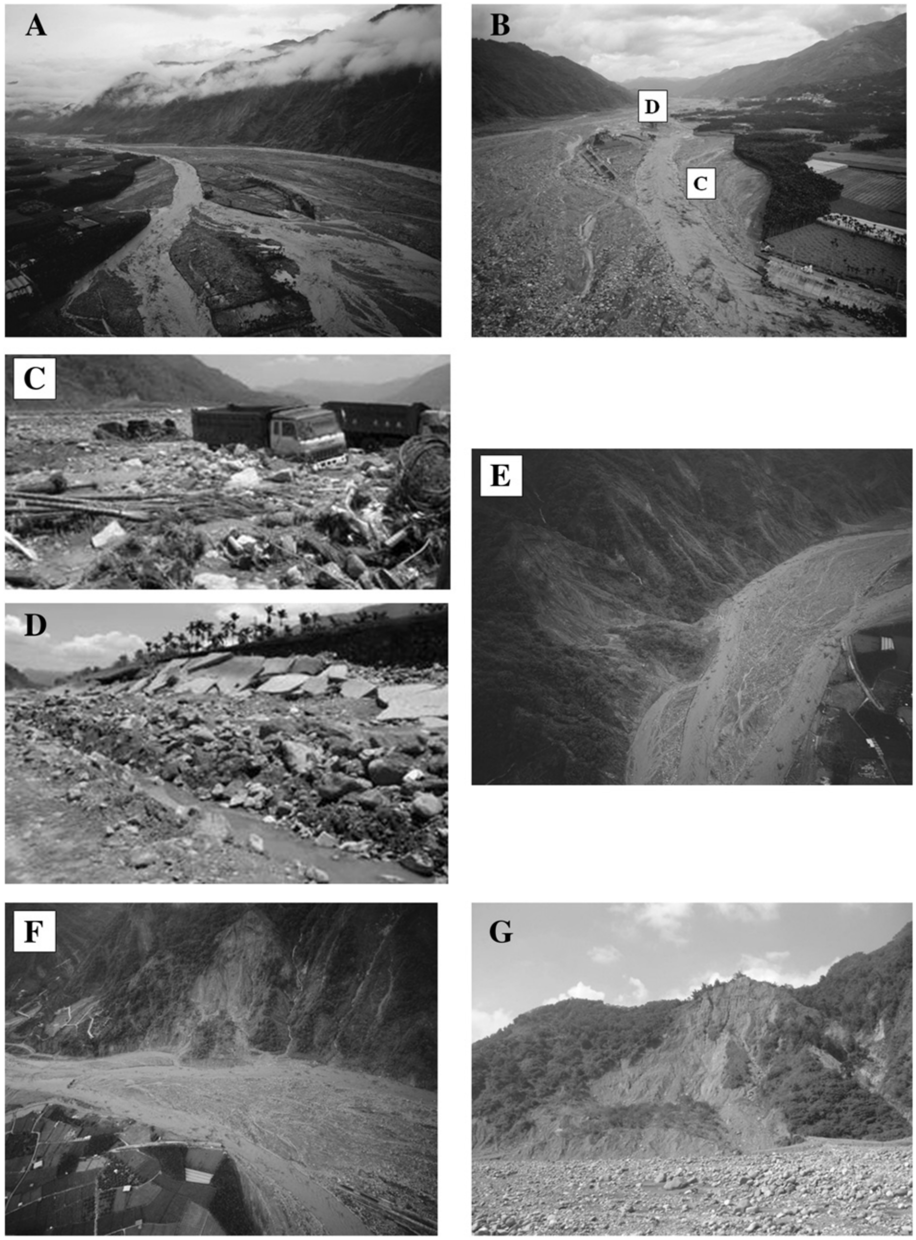

Fig. 5. Aerial photographs of the Shan-An flood with (A) upstream view and (B) downstream view. Photographs of (C) The topped vineyard and (D) The destroyed Shan-An levee. Aerial photographs of the landslide with (E) downstream view and (F) oblique view. (G) Close-view photograph of the landslide taken on the ground.

2002; Ali, 2007). The impact force of debris was considered to an affecting factor to exaggerate the flooding attack. For the quantitative analysis, impacts of water and debris were calculated to modify the simulation results for the levee failure. Impact force onto the levee is composed of flow impact force of water and debris and can be estimated as follows (Kogan, 1997).

$$F_w = \rho_{hc} V_{hc}^2 \tag{1}$$

$$\rho_{hc} = \rho_d c_v + (1 - C_v)\rho_w \tag{2}$$

in which F_w is the impact force of water per unit area (N/m^2), V_{hc} is the velocity of hyper-concentrated sediment fluid (m/s), ρ_{hc} is the density of hyper-concentrated sediment fluid (kg/m^3), ρ_d is the debris density (kg/m^3), ρ_w is the water density (kg/m^3), and C_v is the volumetric concentration (volume of debris/volume of water and debris, dimensionless).

Based on Manning's formula, the flow depth (h) and velocity (V_{hc}) can be calculated for a hyper-concentrated sediment fluid as:

$$h = \left[\frac{nQ_{hc}}{B\sqrt{S}}\right]^{3/5} \tag{3}$$

$$V_{hc} = Q_{hc} / (Bh) \tag{4}$$

in which Q_{hc} is the hyper-concentrated sediment flow (m^3/s), B is the river width (m), S is the river slope (%), and n is Manning coefficient. The hyper-concentrated sediment flow can be obtained by water flow (Q_w) and debris volumetric concentration (C_v) as:

$$Q_{hc} = \frac{1}{1 - C_v} Q_w. \tag{5}$$

Based on on-site testing and observation, the following data were collected as $\rho_d = 2650$ kg/m^3, $\rho_w = 1000$ kg/m^3, $C_v = 0.15$, $B = 300$ m,

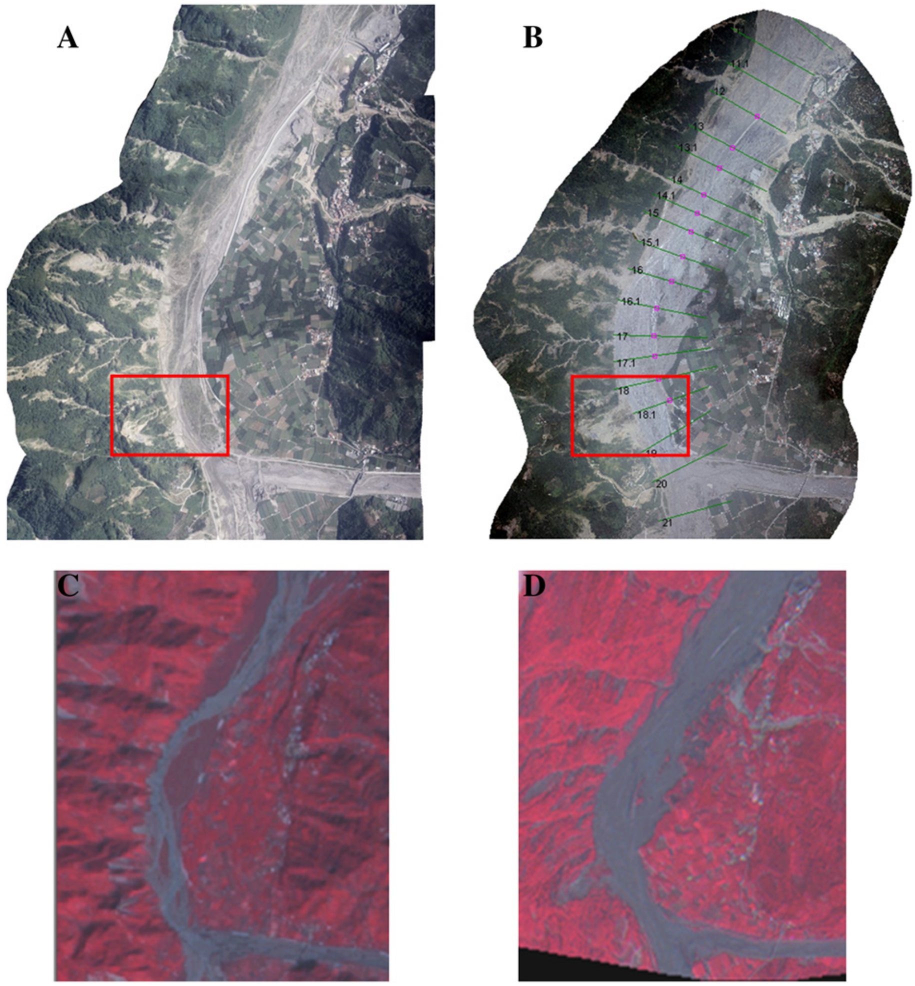

Fig. 6. Aerial photographs and false-color satellite images of Shan-An flood. Many seismic-triggered landslides remaining on the hillslope at the left riverside and Shan-An levee (the white line) at the right side of Chenyulan River in (A) pre-flood aerial photograph. Washed-out Shan-An levee marked in purple dots and the allocation of section surveying and cross-section No. as input into HEC-RAS simulation in (B) post-flood aerial photograph. Comparing (B) with (A), the river width was double and the levee residual was left in the water. False-color satellite images of (C) pre-flood acquired by SPOT-IV and (D) post-flood acquired by FORMOSAT-II showing widening river section apparently after Typhoon Mindulle.

and $S = 1.93\%$. For a hyper-concentrated sediment flow, n has an empirical range between 0.1 and 0.06, and 0.1 is suggested for the front flow and adopted in this paper (PWRIMC, 1988). Subsequently, at the moment of levee collapse with $Q_w = 3200$ cms, the following can be calculated as $\rho_{hc} = 1247.5$ kg/m^3, $Q_{hc} = 3764.7$ cms, $h = 3.7$ m, $V_{hc} = 3.3$ m/s, and $F_w = 14.0$ kN/m^2.

6.3. The impact force of debris (F_d)

For large boulders in the flow, the impact force of the slurry can be estimated as:

$$F_d = C\rho_d A V_s \quad (6)$$

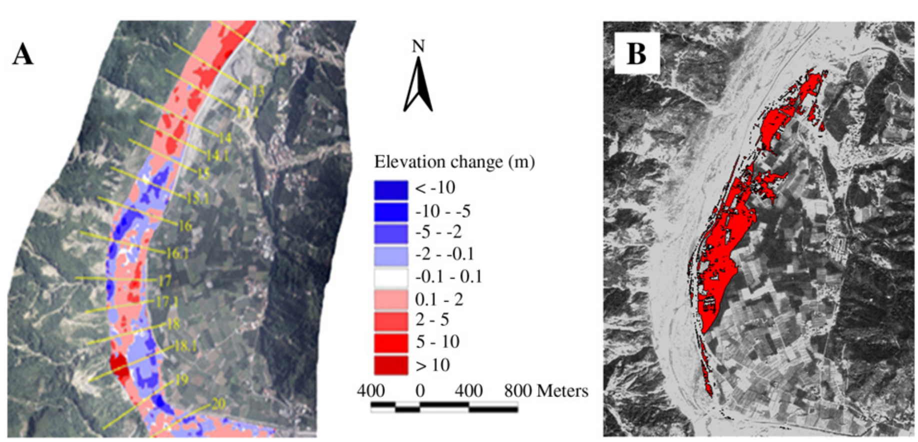

Fig. 7. (A) The elevation change of riverbed measured by comparing pre-flood and post-flood DEMs. (B) The sediment-deposited farmland in red derived by change detection on pre-flood and post-flood satellite images.

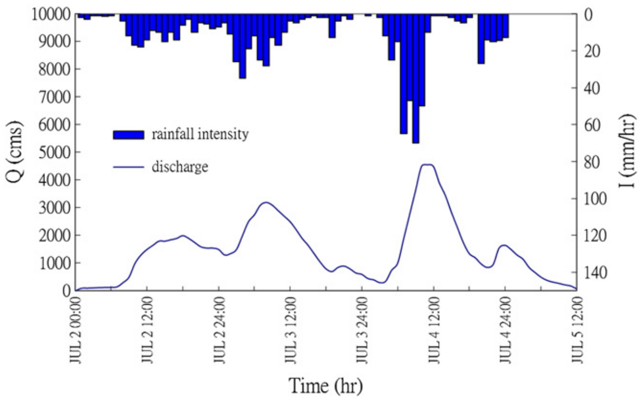

Fig. 8. Flow discharge and rainfall intensity of Chenyulan River at Shan-An levee during Mindulle flood event.

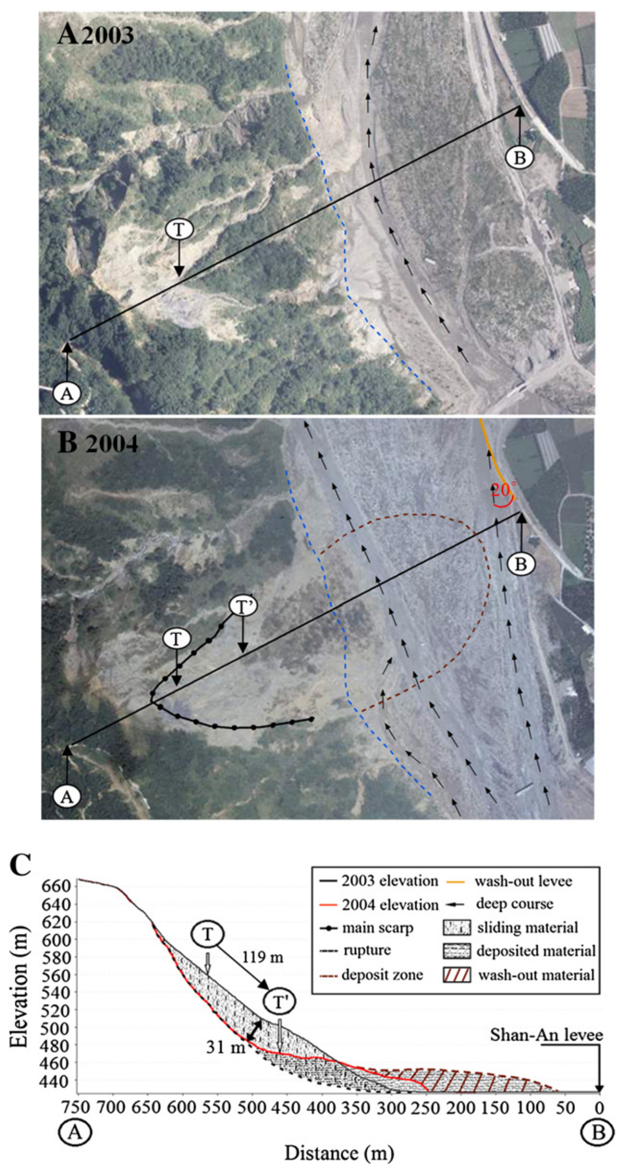

Fig. 9. (A) Pre-flood and (B) post-flood aerial photographs of the landslide shown as the small rectangles in Fig. 6A and B, respectively. (C) The elevation variation of the slope before and after landsliding on A-B section. Solid lines are measurement and dashed lines represent estimate. Main scarp was identified by the differential DEMs. Trees at point T sliding 136 m to point T′ can be easily identified by comparing (A) with (B). The estimated elevation was derived by the equal mass between sliding and deposited materials.

in which F_d is the impact force of debris per unit area (N/m^2), A is contact area (m^2), and C is transmission speed of the elastic wave impacting a rock (usually 4000 m/s) (Cui et al., 2005). Field investigation found many cobbles left on the riverbed and many boulders with a diameter of >0.5 m left in the flooded vineyard (see Figure 5C) which are believed to originally come from the landslide on the left hill. The biggest stones accumulated at the front part of the landslide-induced flood (Takahashi, 2007), so we estimated the contact area A as 0.25 m^2. Based on the on-site observation, and $\rho_d = 2650$ kg/m^3, the impact force of debris per unit area (F_d) can be estimated as 8877 kN/m^2 through Eq. (6). Considering the diversion angle of 20° as shown in Fig. 9B, the impact force of debris to the levee was ~3000 kN/m^2.

In general, the design strength of the concrete levee wall (400 kN/m^2) is beyond the impact force of water (14.0 kN/m^2) but below the impact force of debris (3000 kN/m^2). The earthen levee can allow a flow with a maximum velocity of 1.98 m/s. Once a break occurred on the levee surface, a 3.3 m/s flow running through the earthen body caused a hundred-meter long collapse of Shan-An levee.

7. Conclusions

The finding of both field investigation and scientific analysis was concluded as follows.

1. Flood investigation, including field observation with GPS, photograph interpretation, digital photogrammetry, satellite imagery processing, and terrain surveying, was conducted to provide flooding evidences. Through image processing, the pre- and post-flood aerial and satellite images efficiently illustrate an overall picture of flooding severity at Shan-An region (see Figure 6). According to the image analysis, the elevation change of riverbed photogrammetrically measured by comparing pre-flood and post-flood DEMs, and the inundated area was about 157 ha and the debris-deposited farm was about 40 ha (see Figure 7).
2. To reveal quantitatively the water profile, HEC-RAS was employed to simulate hydraulic conditions under rainfall records during the Mindulle flood event. Chenyulan River had a peak flow of 3200 cms (about 10-year return period) at the time when the levee collapse was reported and another peak flow of 4585 cms (about 20-year return period). Both peak flows were under the design capacity of the Shan-An levee (5850 cms, 100-year return period). The HEC-RAS simulation results reveal that the design strength of Shan-An levee is able to resist the peak flow of Mindulle rainfall and should not cause the overtopping and inundation.
3. More importantly, the seismic-triggered landslide on the left riverside was reactivated by intensive rainfalls. A great amount of soils deposited on the river bed and narrowed down the river Section 18 into 20% to increase the impact force on Shan-An levee. As well as an elevated-up flow surface, the flow was diverted 20° toward Shan-An levee by physical obstruction of landslide deposit to induce a severe attack to the earthen levee and to cause the break and eventually levee collapse.
4. The landslide on the left riverside at Section 18 provided a great source of a high concentrated sediment flow. The impact analysis shows that the design strength (400 kN/m^2) of Shan-An levee should be able to resist the impact of water but not the impact of debris (~3000 kN/m^2).
5. The analysis results suggest that the flow with high concentration of debris increased water pressure to the point that water flowed through the earthen levees with concrete walls. Instead of overtopping, Shan-An levee faced to a catastrophic collapse due to flow scour after the broken concrete wall of levee by debris impact. Once there was a break on the concrete wall, the whole earthen levee was scoured away, which is a typical case of a concrete-surfaced earthen levee collapse.

Acknowledgements

This work was made possible through the thankful help from the 4th River Basin Management Bureau. The topographic data and Lidar image were contributed by Eagles Flying Survey Technology Company. Sincere appreciation also goes to the anonymous reviewers for their constructive comments.

References

Ali, A.M.S., 2007. September 2004 flood event in southwestern Bangladesh: a study of its nature, causes, and human perception and adjustments to a new hazard. Natural Hazards 40, 89–111.

Bisson, M., Favalli, M., Fornaciai, A., Mazzarini, F., Isola, I., Zanchetta, G., Pareschi, M.T., 2005. A rapid method to assess fire-related debris flow hazard in the Mediterranean region: an example from Sicily (southern Italy). International Journal of Applied Earth Observation and Geoinformation 7, 217–231.

Chen, L.C., Liu, Y.C., Chan, K.C., 2006. Integrated community-based disaster management program in Taiwan: a case study of Shang-An village. Natural Hazards 37, 209–223.

Chow, W.T., 1973. Open-Channel Hydraulics. McGraw-Hill Book Company, New York, p. 680.

Cui, P., Chen, X., Wang, Y., Hu, K., Lee, Y., 2005. Jiangjia Ravine debris flow flows in south-western China. In: Jakob, Hungr (Eds.), Debris-Flow Hazards and Related Phenomena. Praxis Publishing Ltd, UK, pp. 565–594.

Dadson, S.J., Hovius, N., Chen, H., Dade, W.B., Hsieh, M.L., Willett, S.D., Hu, J.C., Horng, M.J., Chen, M.C., Stark, C.P., Lague, D., Lin, J.C., 2003. Links between erosion, runoff variability and seismicity in the Taiwan Orogen. Nature 426, 648–651.

Dadson, S.J., Hovius, N., Chen, H., Dade, W.B., Lin, J.C., Hsu, M.L., Lin, C.W., Horng, M.J., Chen, T.C., Milliman, J., Stark, C.P., 2004. Earthquake-triggered increase in sediment delivery form an active mountain belt. Geological 32, 733–736.

Dewitte, O., Jasselette, J.C., Cornet, Y., Van Den Eeckhaut, M., Collignon, A., Poesen, J., Demoulin, A., 2008. Tacking landslide displacements by multi-temporal DTMs: a combined aerial stereophotogrammetric and LIDAR approach in western Belgium. Engineering Geology 99, 11–22.

FEMA, 2006. National Response Plan Main Menu Available: http://www.dhs.gov/dhspublic/interapp/editorial/editorial_0570.xml.

Finley, P.J., Mostyn, G.R., Fell, R., 1999. Landslide risk assessment: prediction of travel distance. Canadian Geotechnical Journal 36, 556–562.

García-Meléndez, E., Molina, I., Ferre-Julià, M., Aguirre, J., 1998. Multisensor data integration and GIS analysis for natural hazard mapping in a semiarid area (southeast Spain). Advances in Space Research 21, 493–499.

Hamandawana, H., Eckardt, F., Chanda, R., 2005. Linking archival and remotely sensed data for long-term environmental monitoring. International Journal of Applied Earth Observation and Geoinformation 7, 284–298.

Kawaike, K., Inoue, K., Toda, K., Nakai, T., 2002. Effects of sediment yield on inundation flow in a hillside city. Journal of Hydroscience and Hydraulic Engineering 20, 151–166.

Knebl, M.R., Yang, Z.L., Hutchison, K., Maidment, D.R., 2005. Regional scale flood modeling using NEXRAD rainfall, GIS, and HEC-HMS/RAS: a case study for the San Antonio river basin summer 2002 storm event. Journal of Environmental Management 75, 325–336.

Kogan, F.N., 1997. Global drought watch from space. Bulletin of the American Metrological Society 78, 621–636.

Macfarlane, D.F., 2009. Observations and predictions of the behaviour of large, slow-moving landslides in schist, Clyde Dam reservoir. New Zealand, Engineering Geology 109, 5–15.

Montoya, L., 2003. Geo-data acquisition through mobile GIS and digital video: an urban disaster management perspective. Environmental Modelling and Software 18, 869–876.

NSPO, 2005. Available: http://www.nspo.org.tw/e60/menu0401.html.

Pappenberger, F., Beven, K., Horritt, M., Blazkova, S., 2005. Uncertainty in the calibration of effective roughness parameters in HER-RAS using inundation and downstream level observations. Journal of Hydrology 302, 46–69.

Piwowar, J.M., Pdeele, D.R., LeDrew, E.F., 1998. Temporal mixture analysis of Arctic Sea ice imagery: a new approach for monitoring environmental change. Remote Sensing of Environment 63, 195–207.

PWRIMC (Public Works Research Institute Ministry of Construction), 1988. Technical Standard for the Measures Against Debris Flow, Sabo (Erosion Control) Division. Public Works Research Institute Ministry of Construction, Japan.

Qi, S., Yan, F., Wang, S., Xu, R., 2006. Characteristics, mechanism and development tendency of deformation of Maoping landslide after commission of Geheyan reservoir on the Qingjiang River, Hubei Province, China. Engineering Geology 86, 37–51.

Sirangelo, B., Braca, G., 2004. Identification of hazard conditions for mudflow occurrence by hydrological model application of FLaIR model to Sarno warning system. Engineering Geology 73, 267–276.

Takahashi, T., 2007. Debris flow. Taylor & Francis, The Netherlands, p. P448.

Teng, J., Sun, M., Huang, W., Yu, F., 2005. Application study on storm surge disaster prevention and reduction based on GIS. Proceedings of IGARSS 2005, Seoul, Korea, 2, pp. 967–970.

Tralli, D.M., Blom, R.G., Zlotnicki, V., Donnellan, A., Evans, D.L., 2005. Satellite remote sensing of earthquake, volcano, flood, landslide and coastal inundation hazards. ISPRS Journal of Photogrammetry and Remote Sensing 59, 185–198.

USACE, 2002. HEC-RAS River Analysis System User's Manual, Version 3.1. Davis, CA.

van der Sande, C.J., de Jong, S.M., de Roo, A.P.J., 2003. A segmentation and classification approach of IKONOS-2 imagery for land cover mapping to assist flood risk and flood damage assessment. International Journal of Applied Earth Observation and Geoinformation 4, 217–229.

Yang, M.D., Su, T.C., Hsu, C.H., Chang, K.C., Wu, A.M., 2007. Mapping of the 26 December 2004 tsunami disaster by using FORMOSAT-2 images. International Journal of Remote Sensing 28, 3071–3091.

Yu, F.C., Chen, C.Y., Chen, T.C., Hung, F.Y., Lin, S.C., 2006. A GIS process for delimitating areas potentially endangered by debris flow. Natural Hazards 37, 169–189.